

Impact craters formed by spinning granular projectiles

Accepted manuscript for Physical Review E, 108, 054904, (2023), DOI:

10.1103/PhysRevE.108.054904,

<https://doi.org/10.1103/PhysRevE.108.054904>

Douglas D. Carvalho, Nicolao C. Lima, and Erick M. Franklin*

*School of Mechanical Engineering,
UNICAMP - University of Campinas,
Rua Mendeleev, 200,
Campinas, SP, Brazil*

(Dated: November 28, 2023)

arXiv:2311.15026v1 [astro-ph.EP] 25 Nov 2023

Abstract

Craters formed by the impact of agglomerated materials are commonly observed in nature, such as asteroids colliding with planets and moons. In this paper, we investigate how the projectile spin and cohesion lead to different crater shapes. For that, we carried out DEM (discrete element method) computations of spinning granular projectiles impacting onto cohesionless grains, for different bonding stresses, initial spins and initial heights. We found that, as the bonding stresses decrease and the initial spin increases, the projectile's grains spread farther from the collision point, and, in consequence, the crater shape becomes flatter, with peaks around the rim and in the center of craters. Our results shed light on the dispersion of the projectile's material and the different shapes of craters found on Earth and other planetary environments.

I. INTRODUCTION

Craters formed by the impact of projectiles are commonly observed in nature, such as km-size asteroids colliding with planets and moons and cm-size seeds falling from trees. While the latter involves very low energies (as low as 10^{-7} J, the equivalent of lighting a LED lamp for approximately 0.0000001 s), the former involves huge energies that surpass that of a hydrogen bomb (from 10^{16} J on). Because those scales differ by more than 23 orders of magnitude, the cratering processes and resulting shapes are not the same in all cases. For example, under small energies (low masses and velocities) the impact results in the partial penetration of the projectile and ejection of ground material, while under large energies it involves also melting and evaporation.

Craters of distinct shape and size have been observed in environments with different ground properties and gravity acceleration [1], so that strong variations occur and a classification is not straightforward [2, 3]. In general, small craters have a bowl shape (also called simple craters, Fig. 1(b)), and, as the craters become larger, they present a flat floor and a central peak or peak rings. For even larger craters, they have, in addition to the flat floor and central peak (or peak rings), external rings that are formed from the partial collapse of steep walls (Fig. 1(d)). For reference, lunar craters with diameters smaller than approximately 10 km are bowl-shaped, those with diameters of the order of 100 km have

* erick.franklin@unicamp.br; Corresponding author

the external rings, flat floor and peak rings, and craters within those values vary between bowl-shaped and flat floor with central peak [1]. Notwithstanding their ubiquitous nature, the mechanisms leading to different crater shapes are far from being completely understood.

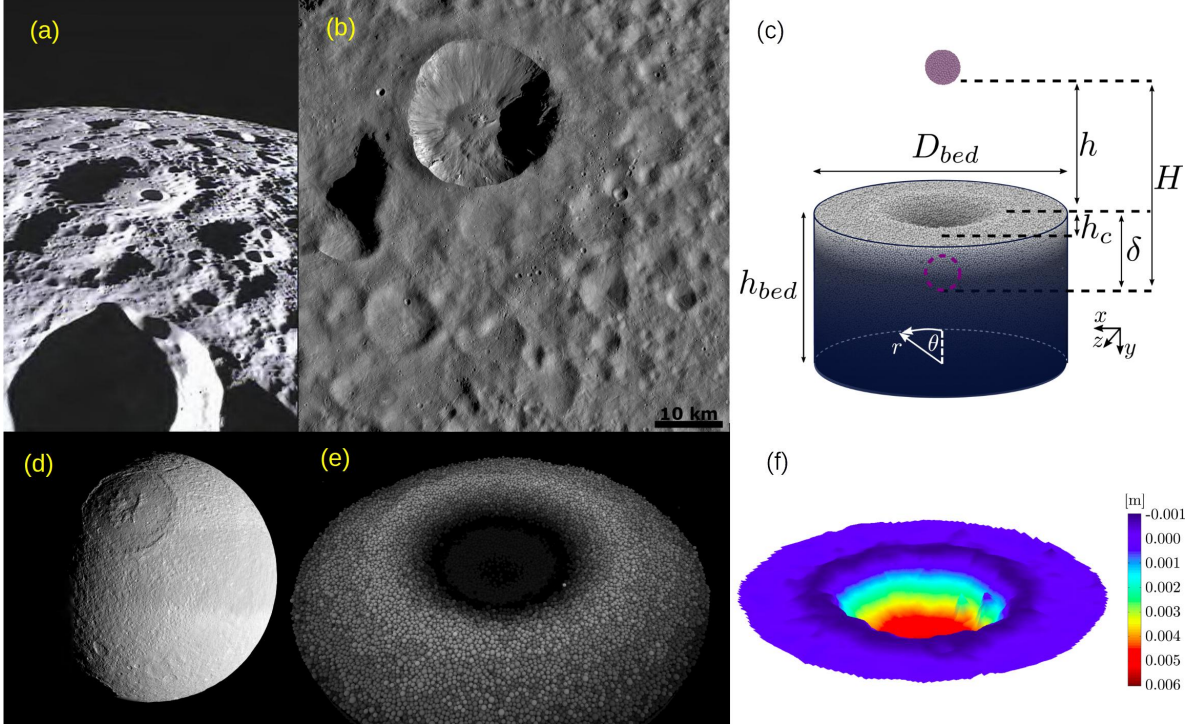


FIG. 1. (a) Craters on Earth's moon (in the middle, with a smaller bowl-shaped crater inside, is Poinsoot crater); (b) Craters on Vesta, with a recent 20-km-diameter crater on the top of image; (c) layout of the numerical setup (the y coordinate points downwards, and, although shown on the bottom, the origin of the coordinate system is on the bed surface centered horizontally in the domain); (d) 445-km-diameter crater on Saturn's moon Tethys; (e) 76-mm-diameter crater obtained numerically from the impact of a 25-mm-diameter steel sphere falling from 50 mm onto a bed of particles (glass spheres with mean diameter of 1 mm); (f) topography (elevation) of a crater formed by a spinning projectile consisting of bonded grains (we notice at least one internal peak close to the rim). In this figure, the bonding stresses are 10^7 N/m², the ratio between linear and angular kinetic energies is 1, and the colorbar shows the elevation from the undisturbed surface (pointing downwards). Images in panels (a), (b) and (d): Courtesy NASA/JPL-Caltech.

Besides the involved energies and sizes, other properties such as the projectile and ground compositions [4], confinement [5], projectile spin [6], and microscopic friction [6] can strongly

influence the crater shape. By using dimensional analysis, Holsapple [7] showed that the dimensionless volume of the crater is a function of two pressure ratios and the density ratio ρ_p/ρ , where ρ_p and ρ are the densities of the projectile and ground materials, respectively. One of the pressure ratios consists of the projectile weight divided by its surface area and normalized by the dynamic pressure,

$$\text{Fr}^{-1} = \frac{D_p g}{V_p^2}, \quad (1)$$

where D_p is the projectile diameter, V_p is the velocity of the projectile at the impact, and g is the modulus of gravity acceleration \vec{g} . This pressure ratio is the equivalent of the inverse of a Froude number Fr^{-1} (gravitational effects compared to inertia), being important in geophysical processes, for which $10^{-6} \lesssim \text{Fr}^{-1} \lesssim 10^{-2}$. Impact cratering is usually considered in the so-called gravity regime when $\text{Fr}^{-1} \lesssim 10^{-2}$, but for cohesionless grains the upper limit is acknowledged to be greater [7].

Because impacts of km-scale asteroids are rare events within the human timescale (every millions of years on Earth's surface, for example), laboratory-scale experiments and numerical simulations have proven essential in the investigation of crater formation [5, 8–16]. By assuring $\text{Fr}^{-1} \lesssim 10^{-1}$ in most cases and using targets consisting of cohesionless grains, those works allowed extrapolations of laboratory results to geophysical problems [17]. For example, Uehara et al. [8, 18] carried out experiments where solid spheres were let to fall onto cohesionless grains for different ρ_p and heights from the bed h , resulting in partially penetrating projectiles (penetration depth $\delta =$ crater depth h_c). They found that the crater diameter D_c varies with $(\rho_p D_p^3 H)^{1/4}$, so that $D_c \sim E^{1/4}$ (the crater diameter varies as a 1/4 power of the energy), where E is the available energy at the impact and $H = h + \delta$ is the total drop distance. They also found that the crater depth h_c does not scale with E , but $h_c \sim H^{1/3}$. In addition, they showed that the diameter of grains and friction and restitution coefficients of the projectile do not affect the crater diameter D_c .

Although most of experiments on impact cratering were for solid projectiles, many problems, in particular in geophysics, concern the impact of aggregates. For example, in the case of asteroids or meteors impacting the surface of a planet, aggregates can be divided into smaller parts which, in their turn, penetrate into the target and excavate the crater. This process can be responsible for the spreading of materials on Earth, just below the ground

surface, such as nickel, platinum and gold [19–21]. The impact of non-spinning aggregates was inquired into by Pacheco-Vázquez and Ruiz-Suárez, who investigated first the sinking of collections of a few intruders in a low-density granular medium [22] and afterwards the impact of aggregates onto a granular bed [4]. They showed that the same scale $D_c \sim h^{1/4}$ found for solid projectiles remains valid, but D_c is larger for aggregates, with a discontinuity accounting for the energy necessary for fragmentation. As a consequence, complex crater shapes that depend on the packing fraction of the projectile appear. They also showed that $h_c \sim h^{1/3}$ is valid only for small energies: h_c decreases abruptly above a threshold value and remains constant for higher energies. Finally, if the fragments once forming the projectile sink in the granular bed (which can happen in low-density beds), they move with a cooperative dynamics [22].

Recently, we [6] carried out 3D (three dimensional) DEM (discrete element method) simulations and showed that the microscopic friction affects considerably the crater morphology. In addition, we showed that differences in initial packing fractions can engender the diversity of scaling laws found in the literature [5, 8, 9, 16, 18], and proposed an *ad hoc* scaling that collapsed our data for the penetration length and can perhaps unify the existing correlations. Finally, we investigated the initial spin of the projectile and showed that both δ and D_c increase with the projectile spin, that large asymmetries can appear depending on the spin axis, and that the final rebound of the projectile is suppressed by the spin.

Even though previous studies explained important aspects of impact cratering, many questions remain open. One of them concerns the mechanics of cratering for spinning aggregates impacting a granular ground. In this specific case, close to impacts observed in nature, the total or partial collapse of projectiles can engender different crater structures, explaining some of the crater shapes observed in nature and how materials from the projectile spread below and over the ground. This paper inquires into these questions. For that, we carried out 3D DEM computations of spinning granular projectiles (aggregates) impacting onto a bed consisting of cohesionless grains, for different bonding stresses (between the projectile’s grains), initial spins and initial heights. We show that, as the bonding stresses decrease and the initial spin increases, the projectile’s grains spread farther from the collision point, and, in consequence, the crater shape becomes flatter, with peaks around the rim and in the center of craters. In addition, we found that the penetration depth of rotating projectiles varies with their angular velocity and degree of collapse (number of detached particles), but

not necessarily with the bonding stresses, indicating that under high spinning velocities the excess of breaking energy contributes only for the larger spreading in the horizontal plane and formation of peaks. Our results shed light on the different shapes of craters found on planets and moons, as well as on the distribution of the projectile material below and over the ground.

II. BASIC EQUATIONS AND NUMERICAL SETUP

As in Ref. [6], we carried out 3D DEM computations [23] using the open-source code LIGGGHTS [24, 25]. The code solves the linear (Eq. (2)) and angular (Eq. (3)) momentum equations for each individual particle at each time step,

$$m \frac{d\vec{u}}{dt} = \vec{F}_c + m\vec{g} , \quad (2)$$

$$I \frac{d\vec{\omega}}{dt} = \vec{T}_c . \quad (3)$$

For each particle, m is the mass, \vec{u} is the velocity, I is the moment of inertia, $\vec{\omega}$ is the angular velocity, \vec{F}_c is the resultant of contact forces between solids, and \vec{T}_c is the resultant of contact torques between solids. The contact forces and torques are computed using the elastic Hertz-Mindlin contact model [26], and we take into account the rolling resistance (please see the Supplemental Material [27] or Ref. [6] for the model description).

The numerical domain consisted of: (i) $N \sim 10^6$ spheres with diameter $0.6 \text{ mm} \leq d \leq 1.4 \text{ mm}$ following a Gaussian distribution and fixed density $\rho = 2600 \text{ kg/m}^3$, which formed a granular bed in a cylindrical container (the distribution of diameters used in the simulations is shown in the Supplemental Material [27]); and (ii) $N_p = 1710$ spheres with $d_p = 1 \text{ mm}$ and $\rho_p = 15523 \text{ kg/m}^3$ bonded together, which formed a round projectile with total diameter $D_p = 0.015 \text{ m}$ and bulk density $\rho_{p,bulk} = 7865 \text{ kg/m}^3$ (packing fraction $\phi_p = 0.507$). Prior to each simulation, around 10^6 grains (bed spheres) were let to fall freely and settle, and grains that were above that height were deleted in order to have a horizontal surface (around 10^4 grains were removed), the number N then depending on the initialization (being always $\sim 10^6$). With that, we obtained a granular bed with diameter $D_{bed} = 125 \text{ mm}$, height $h_{bed} = 76.5 \text{ mm}$, and packing fraction $\phi = 0.554$. For the projectile, the value of ρ_p assured that the agglomerated material had the same size and mass of solid projectiles investigated in [6],

and we applied a given bonding stress σ_p to all grain-grain contacts. In our simulations, σ_p was modeled through a breakup-tension threshold, and we used either $\sigma_p = 1 \times 10^7$, 5×10^7 or 1×10^{32} N/m² in order to investigate the effect of bonding stresses on cratering. The highest value was chosen to avoid the projectile collapse, and the others to have partial or total collapses. The material that bonds two or more particles together can be modeled in several ways [28–31]. In this work, it acts as a spring and damper system, where the bonds can twist, bend, stretch and break due to both normal and tangential stresses. The damping system is based on Guo’s model [28], whereas the bond normal force and the bending and torsional moments are determined using linear models. More details are available in the Supplemental Material [27], and validation and details of the used model can be found in Guo et al. [28] and Schramm et al. [29].

TABLE I. Properties of materials used in the simulations: E is Young’s modulus, ν is the Poisson ratio, and ρ is the material density. The last column corresponds to the diameter of the considered object.

	Material	E (Pa)	ν	ρ (kg/m³)	Diameters (mm)
Bed grains	Sand ^{(1)–(2)}	0.1×10^9	0.3	2600	$0.6 \leq d \leq 1.4$
Projectile grains	-	0.2×10^{11}	0.3	15523	1.0
Bond material	-	0.2×10^{11}	0.3	-	0.1
Walls	Steel ⁽¹⁾	0.2×10^{12}	0.3	7865	125

⁽¹⁾ Ucgul et al. [32–34]

⁽²⁾ Derakhshani et al. [35]

The properties and coefficients of grains forming the bed and projectile were taken from the literature, and are listed in Tabs. I and II (together with those for the walls). In addition, we validated the friction coefficients listed in Tab. II by measuring the angles of repose obtained numerically (details available in Ref. [6]). Because we used spherical particles, we embedded angularity in the rolling friction μ_r (for typical sand, Derakhshani et al. [35] showed that $\mu_r = 0.3$). The simulations began by imposing to the projectile a collision velocity V_p corresponding to the free-fall height h , i.e., $V_p = \sqrt{2gh}$. For the values used in our simulations, Froude numbers were within $3.8 \times 10^{-3} \leq Fr^{-1} \leq 7.5 \times 10^{-2}$, and we used a time step $\Delta t = 1 \times 10^{-7}$ s, which corresponds to less than 10 % of the Rayleigh time

TABLE II. Coefficients used in the numerical simulations.

Coefficient	Symbol	Value
Restitution coefficient (bed grain-bed grain) ⁽¹⁾	ϵ_{gg}	0.60
Restitution coefficient (bed grain-projectile grain) ⁽¹⁾	ϵ_{gp}	0.60
Restitution coefficient (projectile grain-projectile grain) ⁽²⁾	ϵ_{pp}	0.56
Restitution coefficient (bed grain-wall) ⁽¹⁾	ϵ_{gw}	0.60
Restitution coefficient (projectile grain-wall) ⁽¹⁾	ϵ_{pw}	0.60
Fiction coefficient (bed grain-bed grain) ^{(1),(3)}	μ_{gg}	0.52
Friction coefficient (bed grain-projectile grain) ⁽¹⁾	μ_{gp}	0.50
Friction coefficient (projectile grain-projectile grain)	μ_{pp}	0.57
Friction coefficient (bed grain-wall) ⁽¹⁾	μ_{gw}	0.50
Friction coefficient (projectile grain-wall)	μ_{pw}	1.00
Coefficient of rolling friction (bed grain-bed grain) ⁽³⁾	$\mu_{r,gg}$	0.30
Coefficient of rolling friction (bed grain-projectile grain) ⁽¹⁾	$\mu_{r,gp}$	0.05
Coefficient of rolling friction (projectile grain-projectile grain)	$\mu_{r,pp}$	0.30
Coefficient of rolling friction (bed grain-wall) ⁽¹⁾	$\mu_{r,gw}$	0.05
Coefficient of rolling friction (projectile grain-wall)	$\mu_{r,pw}$	1.00

⁽¹⁾ Ucgul et al. [32–34]

⁽²⁾ Zaikin et al. [36]

⁽³⁾ Derakhshani et al. [35]

[35]. Figure 1(c) shows a layout of the numerical setup, and animations showing impacts and cratering are available in the Supplemental Material [27]. The numerical setup of our simulations, output files, and scripts for post-processing the outputs are available in an open repository [37].

III. RESULTS AND DISCUSSION

Figure 2 shows top view images of the final position of grains for non-rotating and rotating projectiles with different bonding stresses σ_p . The bonding stresses are listed on the left, the corresponding elevation (from the undisturbed surface) of each grain is shown on the right,

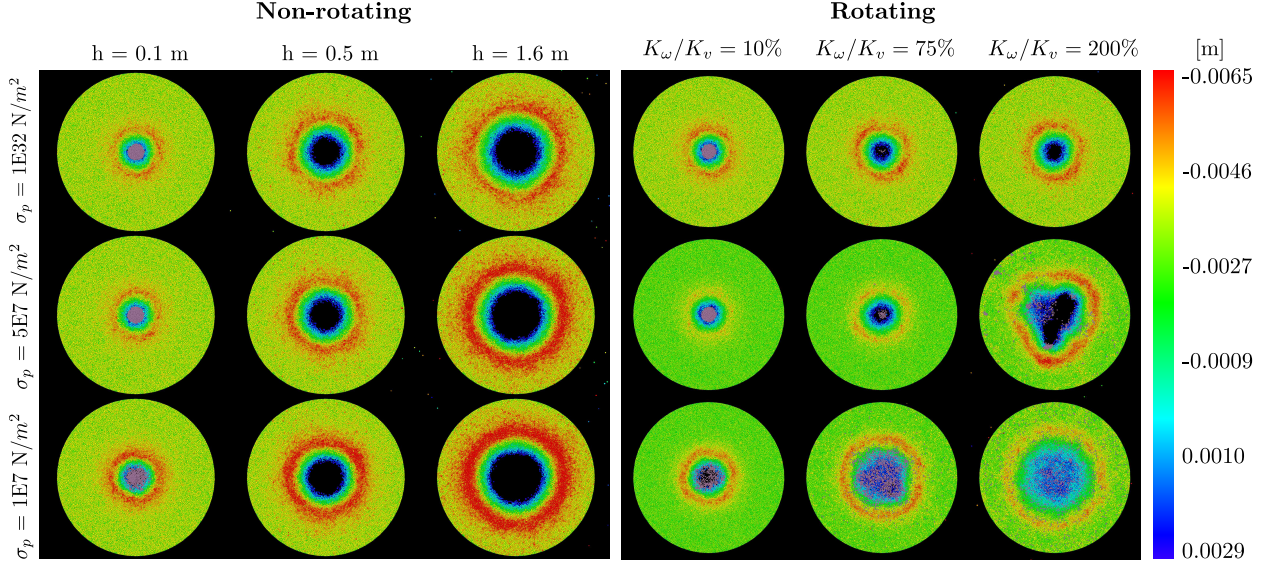


FIG. 2. Top view of final positions of grains, showing the final morphology of craters for non-rotating and rotating projectiles with different bonding stresses. For spinning projectiles, $h = 0.1$ m. The colorbar on the right shows the elevation of each grain from the undisturbed surface (coordinate pointing downwards). The same figure in gray scale is available in the Supplemental Material [27]

and initial heights h (non-rotating cases) and ratios of rotational to linear kinetic energies K_ω/K_v available at the impact (for spinning projectiles) are shown on the top. We used three different values of σ_p : $\sigma_p = 10^{32}$ N/m², which is strong enough to ensure that the agglomerate behaves as a single solid (no breaking) for the range of energies simulated; $\sigma_p = 5 \times 10^7$ N/m², for which the aggregate collapses partially within the ranges of energy simulated; and $\sigma_p = 1 \times 10^7$ N/m², for which the projectile collapses completely for the highest energies simulated. For the non-rotating case, we observe that the crater diameter D_c remains roughly constant and the height of the corona (rim) increases with the decrease in the bonding stresses, and, consequently, with the number of broken bonds (shown next in Fig. 6(c)). In the rotating case, craters are shallower, wider, and with lower rims when compared to the non-rotating case. This is caused by the stronger spreading of grains when the projectile has an initial spin, which we inquire further in the following. In addition, we observe that large asymmetries can appear for rotating cases in which partial breaking occurs, such as when $\sigma_p = 5 \times 10^7$ N/m² and $K_\omega/K_v = 200\%$ (the partial breaking is confirmed in Fig. 6(f)). The asymmetries

come then from a small number of chunks spreading in the horizontal plane (when $\sigma_p = 5 \times 10^7 \text{ N/m}^2$ and $K_\omega/K_v = 200\%$, three large pieces were spread by centrifugal effect, see the Supplemental Material [27] for snapshots of the final positions of grains originally in the projectile and a movie of the entire process).

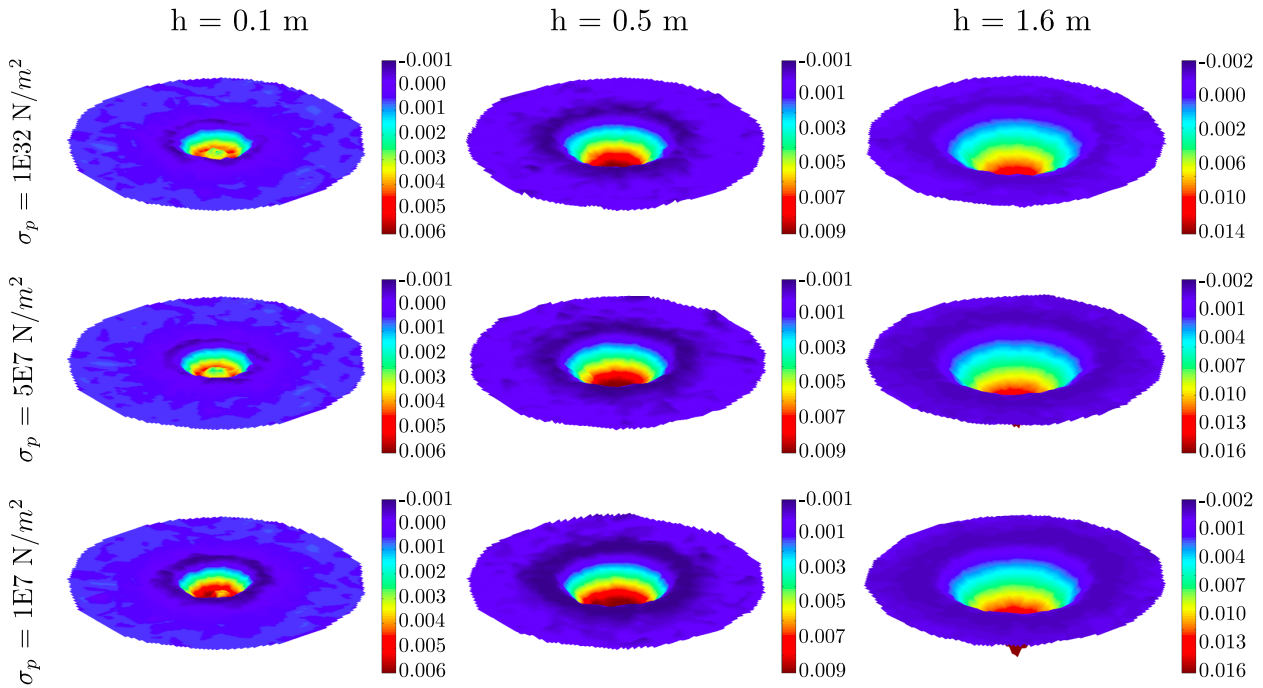


FIG. 3. Topography (elevation) of the final craters for non-rotating projectiles with different bonding stresses. The colorbar on the right of each panel shows the elevation from the undisturbed surface in m . The same figure in gray scale is available in the Supplemental Material [27]

Most of the aforementioned comments can be observed in Figs. 3 and 4, which show the topography (elevation) of the final craters for non-rotating and rotating projectiles, respectively, for the same variations of the bonding stress and available energy of Fig. 2. Although variations of D_c are easier observed in Fig. 2, Figs. 3 and 4 allow for easier and direct observations of the crater depth and the formation of small peaks (we note that the scales of figures are not the same). We notice that the crater shape becomes flatter, with peaks around the rim and in the center of craters as the bonding stresses decrease and the initial spin increases (although peaks can also appear in low-energy cases without fragmentation). Some of these observations are corroborated by Fig. 5, which shows profiles of the elevations of final craters for both non-rotating and rotating projectiles, with different bond-

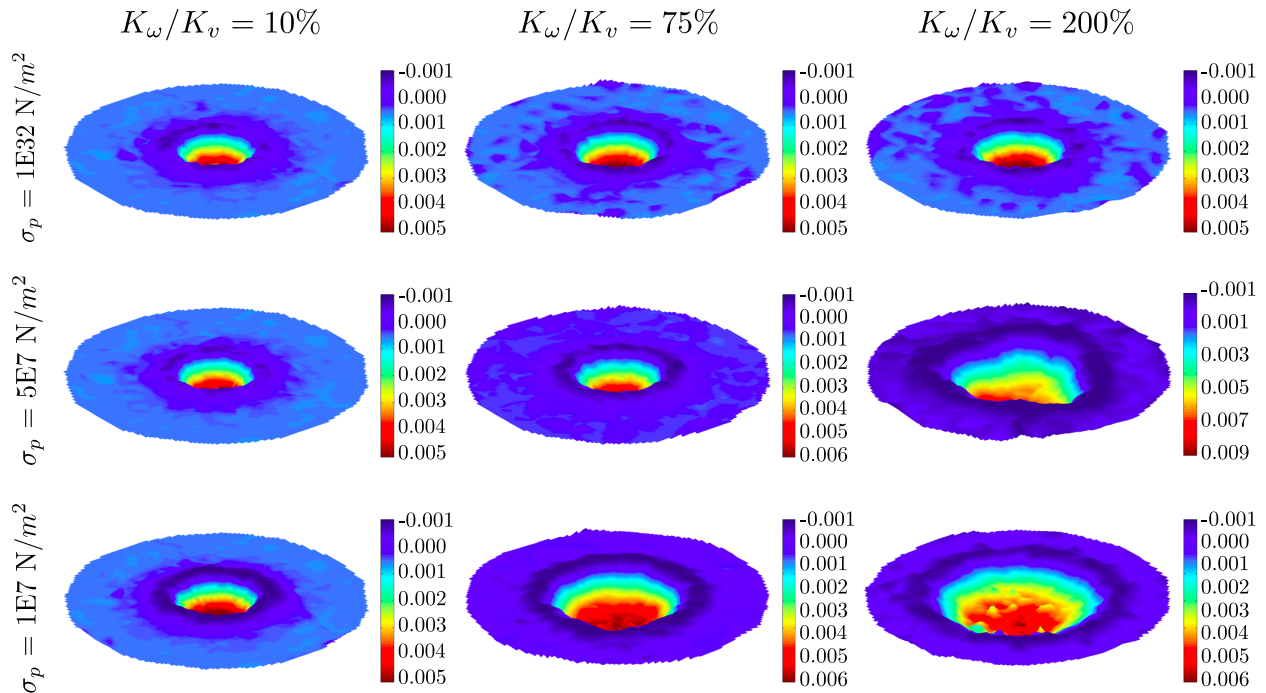


FIG. 4. Topography (elevation) of the final craters for rotating projectiles with different bonding stresses. The colorbar on the right of each panel shows the elevation from the undisturbed surface in m, and $h = 0.1$ m for all panels. The same figure in gray scale is available in the Supplemental Material [27]

ing stresses. Profiles corresponding to different heights are superimposed for non-rotating cases and to different rotational energies for rotating cases, allowing direct comparisons. We observe that craters have higher diameters and lower depths when projectiles have large rotational energies and low bonding stresses, and that some oscillations appear in the region near the corona (corresponding to peripheral peaks). We can observe a central peak in low-energy non-fragmenting cases, but they correspond to the projectile itself (which was not completely buried, see the Supplemental Material [27] for profiles excluding the projectile's grains). Therefore, the final topographies indicate that the formation of central and peripheral peaks are due to the stronger spreading of grains when the projectile has higher rotational energies. In addition, the central peak can also be formed by a partially penetrating projectile when the available energy is relatively low.

In order to inquire further into the crater shape and the level of fracture of the projectile, we plot in Fig. 6 the crater diameter D_c , the penetration depth δ , and the percentage of

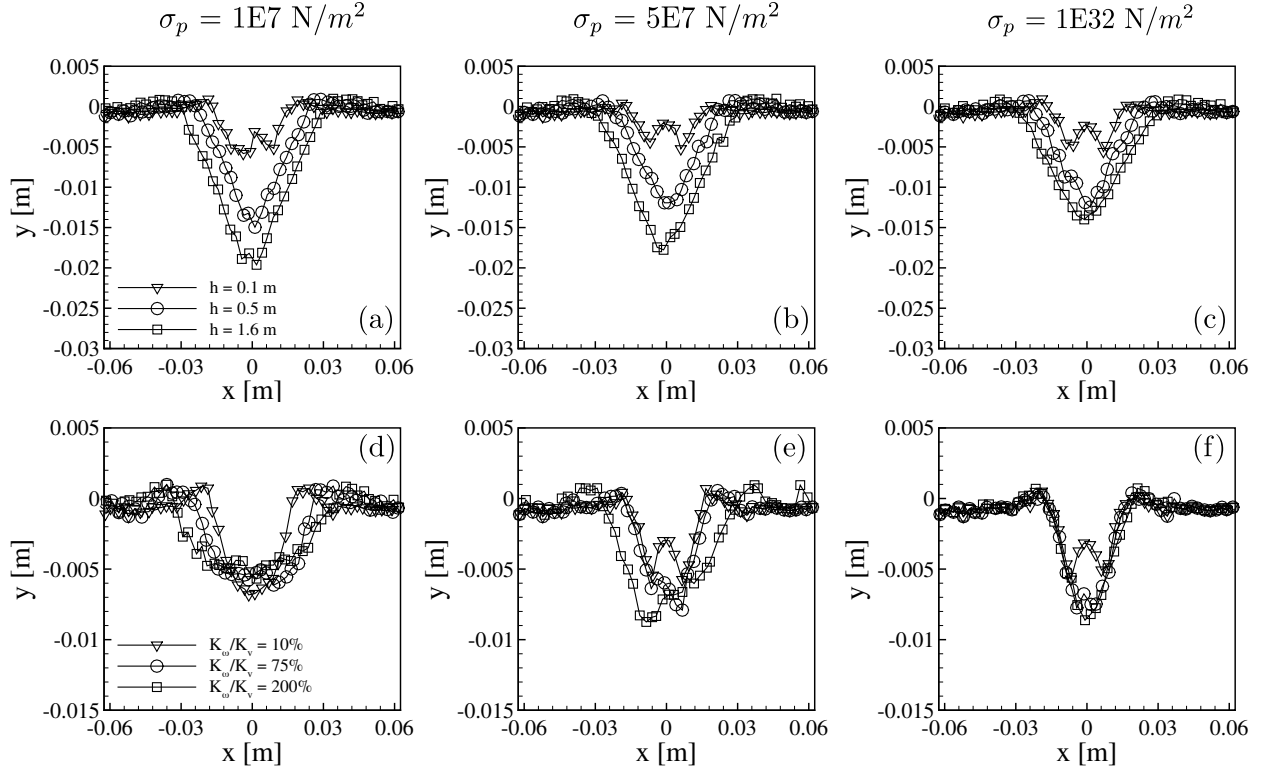


FIG. 5. Profiles of the elevations of final craters for both non-rotating and rotating projectiles, with different bonding stresses. The heights and rotational energies are shown in the figure key, and $h = 0.1$ m for non-rotating projectiles. All profiles were plot in a vertical plane of symmetry (therefore, include the crater center). These profiles include the projectile's grains (see the Supplemental Material [27] for profiles excluding the projectile's grains).

broken bonds as functions of the initial height h or the ratio of rotational to linear kinetic energies K_ω/K_v for, respectively, non-rotating and rotating projectiles. The crater diameter D_c was determined as the diameter of a circle fitted over the corona, and corresponds to an equivalent diameter in the case of asymmetric craters. Whenever the projectile collapsed, we computed δ based on the center of mass of the projectile's grains. For the non-rotating case, we observe that D_c (Fig. 6(a)) is roughly independent of σ_p (for the levels of energy investigated in this paper), varying as $D_c \sim h^{1/4}$, in agreement with Pacheco-Vázquez and Ruiz-Suárez [4], although they measured the packing fraction of agglomerates instead of σ_p (to which we have access in our simulations). However, Pacheco-Vázquez and Ruiz-Suárez [4] identified a discontinuity in D_c as a result of fragmentation, which depended on

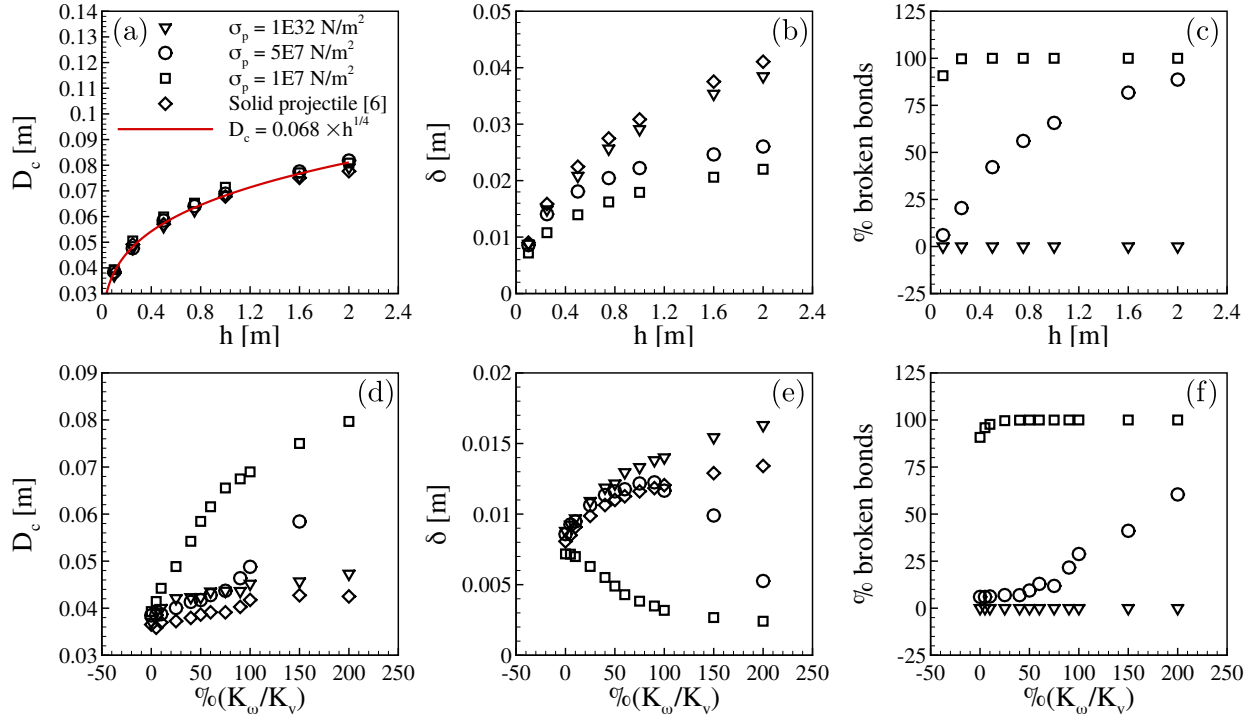


FIG. 6. (a) Crater diameter D_c , (b) penetration depth δ , and (c) the percentage of broken bonds as functions of the initial height h for a non-rotating projectile; panels (d), (e) and (f) show D_c , δ and the percentage of broken bonds as functions K_ω/K_v for spinning projectiles falling from $h = 0.1$ m, respectively. The graphics are parameterized by the bonding stresses (shown in the key of panel (a)), and the results for the solid projectile reported in Carvalho et al. [6] are shown for reference.

the projectile packing fraction. We did not observe the discontinuity, perhaps because our projectiles were lighter than those in Ref. [4] (13.9 g in our simulations, against 33.0–45.5g in their experiments). The penetration depth δ (Fig. 6(b)), on the other hand, depends on σ_p , varying with the percentage of broken bonds (Fig. 6(c)). In addition, the rate of change of δ with h decreases as h increases, and it is possible that a plateau is reached for values of h higher than those simulated in this work. This would be in agreement with the results of Ref. [4], but remains to be investigated further. For δ , Pacheco-Vázquez and Ruiz-Suárez [4] also found a discontinuity resulting from fragmentation, which our simulations did not show. As stated for D_c , the absence of discontinuity is due, perhaps, to the lighter weight of our projectiles. For the rotating case, the situation is different: D_c varies strongly with

σ_p (Fig. 6(d)), and variations for δ are even stronger (Fig. 6(e)). Figure 6(d) shows that D_c increases up to approximately 2 times when σ_p varies from the largest (non-breaking) to the lowest (breaking) values (for K_ω/K_v varying between 0 and 200%), and for moderate stresses ($\sigma_p = 5 \times 10^7$ N/m²) we notice that partial breaking makes D_c to deviate from the curve for the non-breaking case toward to that for the breaking case (which occurs for K_ω/K_v around 100% in Fig. 6(d)). The inverse behavior occurs for δ : it decreases by one order of magnitude when σ_p varies from the largest to the lowest value, with also partial breaking ($\sigma_p = 5 \times 10^7$ N/m²) leading to the breaking case as K_ω/K_v increases. Finally, Fig. 6(f) shows that, indeed, the percentage of broken bonds is 0% for the largest σ_p , and 100% for the lowest σ_p when $K_\omega/K_v \geq 30\%$, while that for moderate σ_p evolves toward 100% for increasing K_ω/K_v . At the same time, values of δ for $\sigma_p = 5 \times 10^7$ N/m² evolve toward those for $\sigma_p = 1 \times 10^7$ N/m² (Fig.6(e)). This implies that the penetration depth of rotating projectiles varies with their angular velocity and degree of collapse (number of detached particles), but not necessarily with the bonding stresses, indicating that under high spinning velocities the excess of breaking energy contributes only for the larger spreading in the horizontal plane and the formation of peaks.

After the impact has occurred, the projectile collapses if the bonding stresses are not strong enough to maintain the agglomerate integrity. In these cases, besides changing considerably the crater shape, the once agglomerated material is spread on or within the ground, over distances that depend on the initial height, bonding stresses and initial spin of the projectile. Understanding how this process occurs can help us, for example, to interpret whether materials found today under the ground have their origin on the ancient impact of asteroids, and how they are distributed, with important applications in geophysics and mining. Therefore, we inquire now into the dispersion of the projectile's grains.

Figure 7 shows the final positions of grains initially forming the projectile, for $\sigma_p = 1 \times 10^7$ N/m² and different K_ω/K_v . The first row (Fig. 7(a)) shows the frequencies of occurrence of the projectile's grains in the r - θ plane (radius-angle plane, independent of the depth), corresponding then to top views of the distributions of the projectile's grains (in the polar plane). We clearly observe that the projectile material reaches distances farther from the collision point as the rotational energy increases. In order to have more quantitative measurements, the second (Fig. 7(b)) and third (Fig. 7(c)) rows show the frequencies of occurrence of final positions in terms of the angle θ and radius r , for all depths, where the

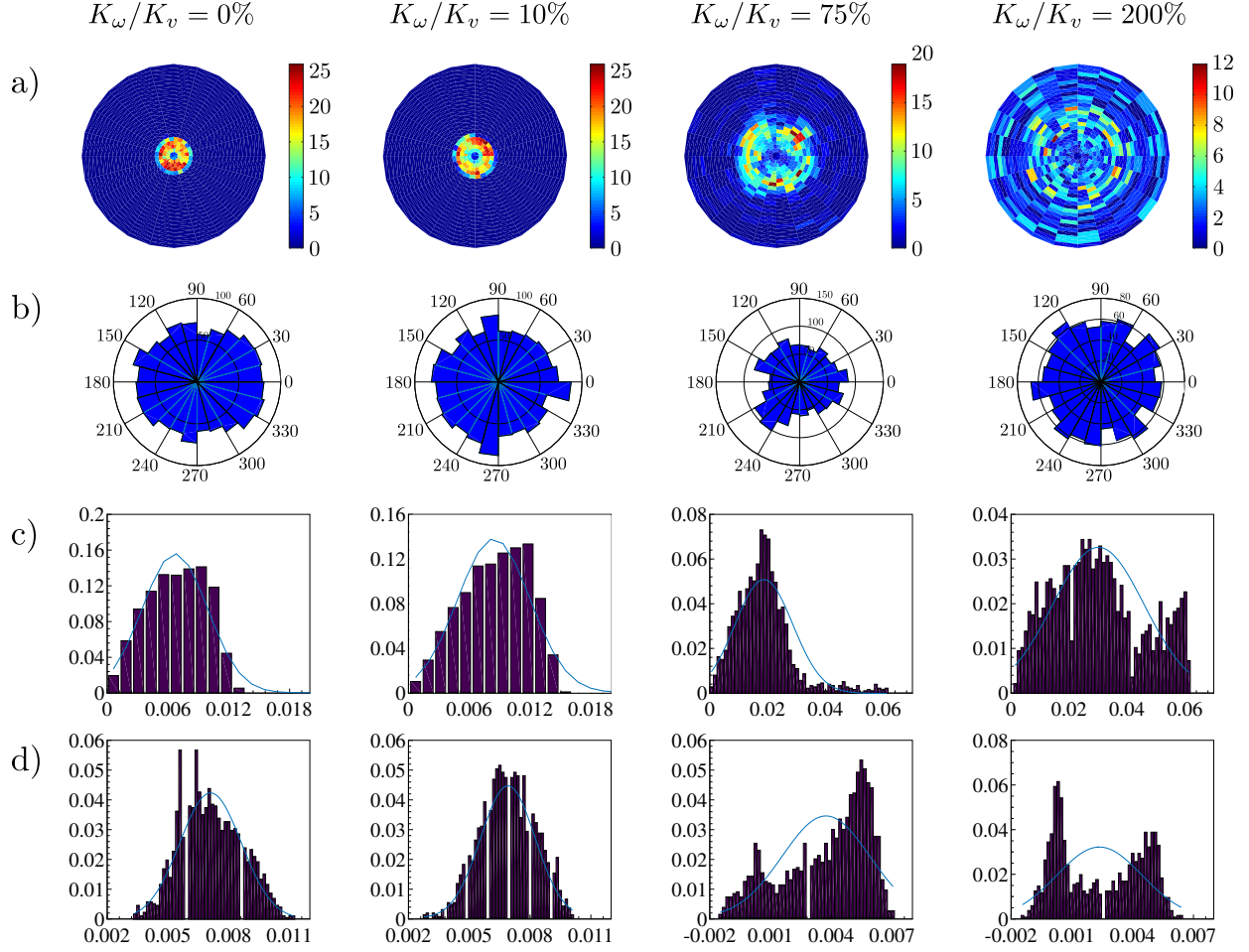


FIG. 7. Final positions the projectile's grains after the impact has taken place, for $\sigma_p = 1 \times 10^7$ N/m² and different values of K_ω/K_v . From top to bottom: (a) Frequencies of occurrence of the projectile's grains in the r - θ plane (radius-angle plane, independent of the depth); (b) frequencies of occurrence of final positions in terms of the angle (all depths); (c) frequencies of occurrence of final positions in terms of radius (all depths); (d) frequencies of occurrence of final positions in the y coordinate (depths for all angles and radii).

angles are given in degrees and the radius in m (see Fig. 1(c) for θ and r). We observe that in this weak-bond case the projectile's grains spread in a roughly symmetrical way along the angles, and distances reached in the radial direction increase with K_ω/K_v : the most probable values of the radius increase from approximately 0.007 m when $K_\omega/K_v = 0$ to 0.03 m (one order of magnitude greater) when $K_\omega/K_v = 200\%$. Finally, the last row (Fig. 7(d)) shows the frequencies of occurrence of final positions in terms of depth (all

angles and radii). Interestingly, we observe that the most probable value decreases with K_ω/K_v , so that in average the projectile's grains tend to remain closer to the surface for higher spinning velocities, different from the behavior of solid projectiles (which reach deeper depths for increasing K_ω/K_v , Ref. [6]). However, the depth distribution widens, so that the projectile's grains populate depths that spans over larger values, including negative ones corresponding to peaks or the corona. Snapshots of the final positions of grains originally in the projectile are available in the Supplemental Material [27].

We note that we did not investigate the effect of initial packing fractions on the dynamics of cratering in this paper (it was the object of Carvalho et al. [6]). However, we measured how the bed packing fraction far from the collision point varies with the linear and rotational energies, for the different bonding stresses used. For that, we selected a 20-mm-height cylindrical region occupying the bottom of the cylindrical container (corresponding to 26% of the container) and measured the average packing fraction before and after the impact. For rotating projectiles, we found no change at all in the packing fraction, while negligible variations (increasing with h) were measured for non-rotating projectiles. The maximum variations were of 0.34%, 0.30% and 0.20% for $\sigma_p = 10^7$, 5×10^7 and 10^{32} , respectively, and $h = 2$ m. We also note that, under some conditions, the dynamics of both cratering and projectile fragmentation change with the stiffness of grains and bonds. Due to the presence of bonds, the effect of stiffness is rather complex and needs to be investigated further.

IV. CONCLUSIONS

In this paper, we investigated numerically how the projectile spin and cohesion lead to different crater shapes, and how the projectile's materials spread over and below the ground. We found that, as the bonding stresses decrease and the initial spin increases: (i) the projectile's grains spread radially farther from the collision point; (ii) the projectile's grains remain in average closer to the surface (lower penetration depths), but spread horizontally over longer distances, with some grains buried deep in the bed while others are above the surface populating peaks or the corona; (iii) as a consequence, the crater shape becomes flatter, with peaks around the rim and in the center of craters. In addition, we found that the penetration depth of rotating projectiles varies with their angular velocity and degree of collapse (number of detached particles), but not necessarily with the bonding stresses

themselves, indicating that under high spinning velocities the excess of breaking energy contributes only for the larger spreading in the horizontal plane and formation of peaks. Our results represent a significant step for understanding how cratering occurs, helping us, for example, to interpret whether materials found today under the ground have their origin on the ancient impact of asteroids, and how they are distributed, with important applications in geophysics and engineering.

V. ACKNOWLEDGMENTS

The authors are grateful to the São Paulo Research Foundation – FAPESP (Grants No. 2018/14981-7, No. 2019/20888-2 and No. 2020/04151-7) and Conselho Nacional de Desenvolvimento Científico e Tecnológico – CNPq (Grant No. 405512/2022-8) for the financial support provided.

-
- [1] H. J. Melosh and B. A. Ivanov, Impact crater collapse, *Ann. Rev. Earth Pl. Sc.* **27**, 385 (1999).
 - [2] N. G. Barlow, S. N. Ferguson, R. M. Horstman, and A. Maine, Comparison of central pit craters on mars, mercury, ganymede, and the saturnian satellites, *Meteorit. Planet. Sci.* **52**, 1371 (2017).
 - [3] R. E. Arvidson, Morphologic classification of martian craters and some implications, *Icarus* **22**, 264 (1974).
 - [4] F. Pacheco-Vázquez and J. C. Ruiz-Suárez, Impact craters in granular media: Grains against grains, *Phys. Rev. Lett.* **107**, 218001 (2011).
 - [5] A. Seguin, Y. Bertho, and P. Gondret, Influence of confinement on granular penetration by impact, *Phys. Rev. E* **78**, 010301 (2008).
 - [6] D. D. Carvalho, N. C. Lima, and E. M. Franklin, Roles of packing fraction, microscopic friction, and projectile spin in cratering by impact, *Phys. Rev. E* **107**, 044901 (2023).
 - [7] K. A. Holsapple, The scaling of impact processes in planetary sciences, *Ann. Rev. Earth Pl. Sc.* **21**, 333 (1993).
 - [8] J. S. Uehara, M. A. Ambroso, R. P. Ojha, and D. J. Durian, Low-speed impact craters in loose granular media, *Phys. Rev. Lett.* **90**, 194301 (2003).

- [9] A. M. Walsh, K. E. Holloway, P. Habdas, and J. R. de Bruyn, Morphology and scaling of impact craters in granular media, *Phys. Rev. Lett.* **91**, 104301 (2003).
- [10] M. P. Ciamarra, A. H. Lara, A. T. Lee, D. I. Goldman, I. Vishik, and H. L. Swinney, Dynamics of drag and force distributions for projectile impact in a granular medium, *Phys. Rev. Lett.* **92**, 194301 (2004).
- [11] H. Katsuragi and D. Durian, Unified force law for granular impact cratering, *Nature Phys.* **3**, 420 (2007).
- [12] S. J. de Vet and J. R. de Bruyn, Shape of impact craters in granular media, *Phys. Rev. E* **76**, 041306 (2007).
- [13] D. I. Goldman and P. Umbanhowar, Scaling and dynamics of sphere and disk impact into granular media, *Phys. Rev. E* **77**, 021308 (2008).
- [14] A. Seguin, Y. Bertho, P. Gondret, and J. Crassous, Sphere penetration by impact in a granular medium: A collisional process, *EPL (Europhysics Letters)* **88**, 44002 (2009).
- [15] P. Umbanhowar and D. I. Goldman, Granular impact and the critical packing state, *Phys. Rev. E* **82**, 010301 (2010).
- [16] H. Katsuragi and D. J. Durian, Drag force scaling for penetration into granular media, *Phys. Rev. E* **87**, 052208 (2013).
- [17] J. C. Ruiz-Suárez, Penetration of projectiles into granular targets, *Rep. Prog. Phys.* **76**, 066601 (2013).
- [18] J. S. Uehara, M. A. Ambroso, R. P. Ojha, and D. J. Durian, Erratum: Low-speed impact craters in loose granular media [*phys. rev. lett.prltao0031-9007* 90, 194301 (2003)], *Phys. Rev. Lett.* **91**, 149902 (2003).
- [19] R. Ganapathy, A major meteorite impact on the earth 65 million years ago: Evidence from the cretaceous-tertiary boundary clay, *Science* **209**, 921 (1980).
- [20] Z. Sawlowicz, Iridium and other platinum-group elements as geochemical markers in sedimentary environments, *Palaeogeogr. Palaeoclimatol.* **104**, 253 (1993).
- [21] I. McDonald, M. Andreoli, R. Hart, and M. Tredoux, Platinum-group elements in the Morokweng impact structure, South Africa: Evidence for the impact of a large ordinary chondrite projectile at the Jurassic-Cretaceous boundary, *Geochim. Cosmochim. Acta.* **65**, 299 (2001).
- [22] F. Pacheco-Vázquez and J. Ruiz-Suárez, Cooperative dynamics in the penetration of a group of intruders in a granular medium, *Nat. Commun.* **1** (2010).

- [23] P. A. Cundall and O. D. Strack, A discrete numerical model for granular assemblies, *Géotechnique* **29**, 47 (1979).
- [24] C. Kloss, C. Goniva, A. Hager, S. Amberger, and S. Pirker, Models, algorithms and validation for opensource dem and cfd-dem, *Prog. Comput. Fluid Dy.* **12**, 140 (2012).
- [25] R. Berger, C. Kloss, A. Kohlmeyer, and S. Pirker, Hybrid parallelization of the LIGGGHTS open-source DEM code, *Powder Technol.* **278**, 234 (2015).
- [26] A. Di Renzo and F. P. Di Maio, Comparison of contact-force models for the simulation of collisions in DEM-based granular flow codes, *Chem. Eng. Sci.* **59**, 525 (2004).
- [27] See Supplemental Material at [URL to be inserted by publisher] for additional graphics for the remaining data, and movies showing the motion of grains and the granular temperature as a projectile impacts a cohesionless granular bed.
- [28] Y. Guo, C. Wassgren, B. Hancock, W. Ketterhagen, and J. Curtis, Validation and time step determination of discrete element modeling of flexible fibers, *Powder Technol.* **249**, 386 (2013).
- [29] M. Schramm, M. Z. Tekeste, C. Plouffe, and D. Harby, Estimating bond damping and bond young's modulus for a flexible wheat straw discrete element method model, *Biosyst. Eng.* **186**, 349 (2019).
- [30] X. Chen, L. Wang, J. Morrissey, and J. Y. Ooi, DEM simulations of agglomerates impact breakage using Timoshenko beam bond model, *Granular Matter* **24** (2022).
- [31] Z. Gong, Y. Yang, L. Cui, J. He, and X. Liu, Dem investigation on the size effect in the fragmentation of intact aggregates, *Powder Technol.* **425**, 118585 (2023).
- [32] M. Ucgul, J. M. Fielke, and C. Saunders, 3D DEM tillage simulation: Validation of a hysteretic spring (plastic) contact model for a sweep tool operating in a cohesionless soil, *Soil Till. Res.* **144**, 220 (2014).
- [33] M. Ucgul, J. M. Fielke, and C. Saunders, Three-dimensional discrete element modelling of tillage: Determination of a suitable contact model and parameters for a cohesionless soil, *Biosyst. Eng.* **121**, 105 (2014).
- [34] M. Ucgul, J. M. Fielke, and C. Saunders, Three-dimensional discrete element modelling (dem) of tillage: Accounting for soil cohesion and adhesion, *Biosyst. Eng.* **129**, 298 (2015).
- [35] S. M. Derakhshani, D. L. Schott, and G. Lodewijks, Micro-macro properties of quartz sand: Experimental investigation and DEM simulation, *Powder Technol.* **269**, 127 (2015).

- [36] O. Zaikin, A. Korablin, N. Dyulger, and N. Barnenkov, Model of the relationship between the velocity restitution coefficient and the initial car velocity during collision, *Transp. Res. Proc.* **20**, 717 (2017).
- [37] N. C. Lima, D. D. Carvalho, and E. M. Franklin, LIGGGHTS input and output files, and Octave scripts for post-processing the outputs are available on Mendeley Data, <http://dx.doi.org/10.17632/d49b9p6f4r.1> (2023).